

# EMD and Teager–Kaiser energy applied to hydrocarbon detection in a carbonate reservoir

Ya-juan Xue,<sup>1,2,3</sup> Jun-xing Cao<sup>1,3</sup> and Ren-fei Tian<sup>3,4</sup>

<sup>1</sup>State Key Laboratory of Oil and Gas Reservoir Geology and Exploitation, Chengdu University of Technology, Chengdu 610059, China.  
E-mail: [xueyj0869@163.com](mailto:xueyj0869@163.com)

<sup>2</sup>College of Communication Engineering, Chengdu University of Information Technology, Chengdu 610225, China

<sup>3</sup>College of Geophysics, Chengdu University of Technology, Chengdu 610059, China

<sup>4</sup>Postdoctoral Workstation of Sinopec Henan Oilfield Company, Zhengzhou 450046, China

Accepted 2013 December 31. Received 2013 December 31; in original form 2013 May 23

## SUMMARY

Oil and gas reservoirs can cause anomalies in the energy and frequency of seismic signals. We can take advantage of these anomalies for hydrocarbon detection. Based on the Teager–Kaiser (TK) energy characteristics, a method that uses this energy in association with the Empirical Mode Decomposition (EMD) method is proposed for hydrocarbon detection in carbonate reservoirs. The EMD method, which can decompose the original seismic signals into a finite number of monocomponent intrinsic mode functions (IMFs) in the temporal domain, is used for multiband filtering. A TK energy separation algorithm is used to estimate the instantaneous frequency and amplitude of the selected IMFs from the EMD method. The proposed method can generate a joint time–frequency representation that can reflect the energy tracking of the seismic signals. The instantaneous spectrums produced by the EMD/TK method have the capability to detect hydrocarbon. The model results to the gas field, which located in the eastern Ordos Basin, China, show that the EMD/TK method can be adopted and they detect the gas-bearing reservoir efficiently. Application of the EMD/TK method in hydrocarbon detection in a gas field located in the Eastern Ordos Basin shows its effectiveness. The EMD/TK method can be used as a new analysis tool to determine the instantaneous spectral properties of a reservoir to detect hydrocarbon.

**Key words:** Time-series analysis; Seismic attenuation; Asia.

## 1 INTRODUCTION

Spectral decomposition is widely used for reservoir characterization, hydrocarbon detection, complex faults and other tasks (Chakraborty & Okaya 1995; Castagna *et al.* 2003; Sinha *et al.* 2005; de Matos & Johann 2007; de Matos *et al.* 2009; Wu & Liu 2009; Huang *et al.* 2011; Ehrhardt *et al.* 2012). Strong amplitude anomalies at specific frequencies can be easily found by using spectral decomposition. As a spectral decomposition method, the Empirical Mode Decomposition (EMD) method, combined with Hilbert Spectral Analysis (HSA), known as Hilbert-Huang Transform (HHT), which was proposed by Huang *et al.* (1998), has been used in seismic signal processing. The EMD method can decompose the original signal into a finite number of intrinsic mode functions (IMFs) from high frequency to low frequency to a monotonous trend with relatively narrow band signals (Huang *et al.* 1998; Magrin-Chagnolleau & Baraniuk 1999; Hassan 2005; Macelloni *et al.* 2011). The EMD method decomposes signals based on the timescale characteristics of the data itself, without any pre-set base function. HSA is used to calculate the instantaneous frequencies (IFs) and the

instantaneous amplitudes (IAs) of the IMFs. The final presentation of the EMD combined with HSA is a time–frequency–energy representation. This method has unique advantages over the commonly used spectral decomposition methods based on Fourier analysis and wavelet transform (Battista *et al.* 2007; Huang *et al.* 2011; Ehrhardt *et al.* 2012). However, once we have the monocomponent functions by EMD, there are still limitations on applying Hilbert Transform (HT) to IMF for physically meaningful IF as stipulated by the well-known Bedrosian and Nuttall theorems (Bedrosian 1963; Nuttall & Bedrosian 1966; Huang *et al.* 2009).

Teager Energy is an energy operator introduced by Teager (1990); its discrete form is given by Kaiser (1990). This algorithm, which estimates local non-linear energy valid for monofrequency signals, has since been called Teager–Kaiser (TK) energy. TK energy is usually used to study non-linear processes such as speech recognition, noise suppression, image enhancement and edge detection. de Matos showed that the seismic wave energy is directly associated with the physical model used by Kaiser (de Matos & Johann 2007; de Matos *et al.* 2008, 2009). However, the original TK energy approach is not valid for seismic signals, which have multifrequency

components. As suggested by the Kaiser (1990) results, the signals should be bandpass filtered before calculating the TK energy.

The TK energy operator can be used by the energy separation algorithm (ESA) to estimate the IFs and IAs of the monofrequency signals (Maragos *et al.* 1993). ESA is valid for AM–FM signal demodulation, and it yields very small errors. It was confirmed that ESA has better time resolution and faster instantaneously adapting nature and smaller computational complexity than the HT (Potamianos & Maragos 1994).

Having employed EMD to produce IMF, Huang *et al.* test TK energy operator on non-stationary and non-linear data for the first time and make the EMD combined TK operator well suited for non-stationary signals analysis (Huang *et al.* 2009). Hereafter, the EMD combined TK operator is applied to sonar target recognition, fault diagnosis of bearings and so on. In this paper, we introduce the EMD method combined with the TK ESA to seismic signals and further extend this method to a spectral decomposition technology and apply the EMD/TK method to seismic data acquired over a carbonate reservoir in China.

## 2 PRINCIPLE AND METHODS

### 2.1 EMD

Huang *et al.* believe that only the IF of an IMF has physical meaning (Huang *et al.* 1998, 2009). EMD is based on the simple assumption that any data consist of different simple intrinsic modes of oscillations (Huang *et al.* 1998). Each of these oscillatory modes is represented by an IMF with the following definition:

- (1) In the whole signal segment, the number of extrema and the number of zero-crossings must either equal or differ at most by one, and
- (2) At any point, the mean value of the envelope defined by the local maxima and the envelope defined by the local minima is zero.

The first condition of the IMF definition is similar to the narrow-band requirement for a stationary Gaussian process. The second condition uses a local requirement instead of a global one which guarantees that the unwanted fluctuations induced by a symmetric waveform will not be emerged in the IF.

The IMF definition shows that the internal vibration modes of the data are characterized by the IMFs. Each IMF involves only one mode of oscillation. The oscillation will also be symmetric with respect to the ‘local mean’. The IMF, linear or non-linear, can have constant amplitude and frequency as in a simple harmonic component or have variable amplitude and frequency as functions of time. EMD resolved one key obstacle for computing a meaningful IF from a multicomponent signal by reducing it to a collection of monocomponent functions (Huang *et al.* 2009). The final complicated signal is formed by the overlaps of IMFs. The purpose of EMD is to obtain IMFs. IMFs decomposed by the EMD method can be defined and distinguished according to the delay between the adjacent extreme points of the signal itself through a sifting process.

Huang *et al.* state that with the objective of obtaining a detailed, yet empirical, statistical knowledge of the EMD behaviour, EMD is just as we might do for some unknown ‘filter’ in signal processing (Huang & Shen 2005). It has been proven that the EMD method essentially acts as a dyadic filter bank resembling those involved in wavelet decomposition (Flandrin *et al.* 2004). Wang *et al.* also find that numerical examples of Gaussian bandpass noise indicate that

EMD acts as an adaptive, multiband overlapping filter bank (Wang *et al.* 2012).

The steps of the EMD method to decompose the signal into IMFs are as follows:

- (1) Identify all the extreme points of the time-series signal  $X(t)$ , fitting the upper envelope  $u(t)$  with all the maximum points of  $X(t)$ , and fitting the lower envelope  $v(t)$  with all the minimum points of  $X(t)$ , meeting

$$v(t) \leq X(t) \leq u(t). \quad (1)$$

Then, the average curve for the upper and lower envelopes is

$$m(t) = [u(t) + v(t)]/2. \quad (2)$$

Let  $h_1(t) = X(t) - m(t)$ ; then,  $h_1(t)$  is the IMF.

- (2) Due to the overshoot and the subduction, the envelope spline approximation will produce a new extreme value that influences the location and size of the original extreme points. Thus,  $h_1(t)$  does not fully meet the IMF conditions. To obtain the required  $h_1(t)$ , let  $h_1(t)$  replace  $X(t)$ . Corresponding with  $h_1(t)$ , the upper envelope is  $u_1(t)$ , and the lower envelope is  $v_1(t)$ . Then, repeat the process:

$$m_1(t) = [u_1(t) + v_1(t)]/2,$$

$$h_2(t) = h_1(t) - m_1(t),$$

.....

$$m_{k-1}(t) = [u_{k-1}(t) + v_{k-1}(t)]/2,$$

$$h_k(t) = h_{k-1}(t) - m_{k-1}(t).$$

The process is repeated until every  $h_k(t)$  meets the IMF conditions. Then, the first IMF  $C_1(t)$  and the remaining part of the signal  $r_1(t)$  are obtained:

$$C_1(t) = h_k(t),$$

$$r_1(t) = X(t) - C_1(t).$$

- (3) EMD is continuously used on the remaining part of the signal. The decomposition proceeds until either the remaining part of the signal is monotonous or its value is less than the predetermined value. After decomposition, the resultant IMFs and the margin are:  $r_2(t) = r_1(t) - C_2(t), \dots, r_n(t) = r_{n-1}(t) - C_n(t)$ .

The original signal  $X(t)$  can be expressed as the sum of the IMFs and the margin:

$$X(t) = C_1(t) + C_2(t) + \dots + C_n(t) + r_n(t). \quad (3)$$

Fig. 1 shows a mean spline produced by the average of the upper and lower envelope of a signal. The upper and lower envelopes of a signal are produced by the two cubic spline curve fits by first locating the extrema of a signal. Tied to the assumptions, EMD has a number of limitations in implementing the algorithm (Huang & Shen 2005; Huang & Wu 2008; Rato *et al.* 2008). For end effects suppressing, although there are many methods to adopt, we have chosen the simple method of Huang *et al.* (1998) to avoid the end effects in our applications because there are always a large amount of seismic data to process in reservoir prediction. Otherwise, mode mixing phenomenon is also a limitation in the EMD sifting process. Mode mixing phenomenon implies that a signal may reside in different IMF components or an IMF may include different scales of signals. Thus, the IMFs that resulted from the EMD method will

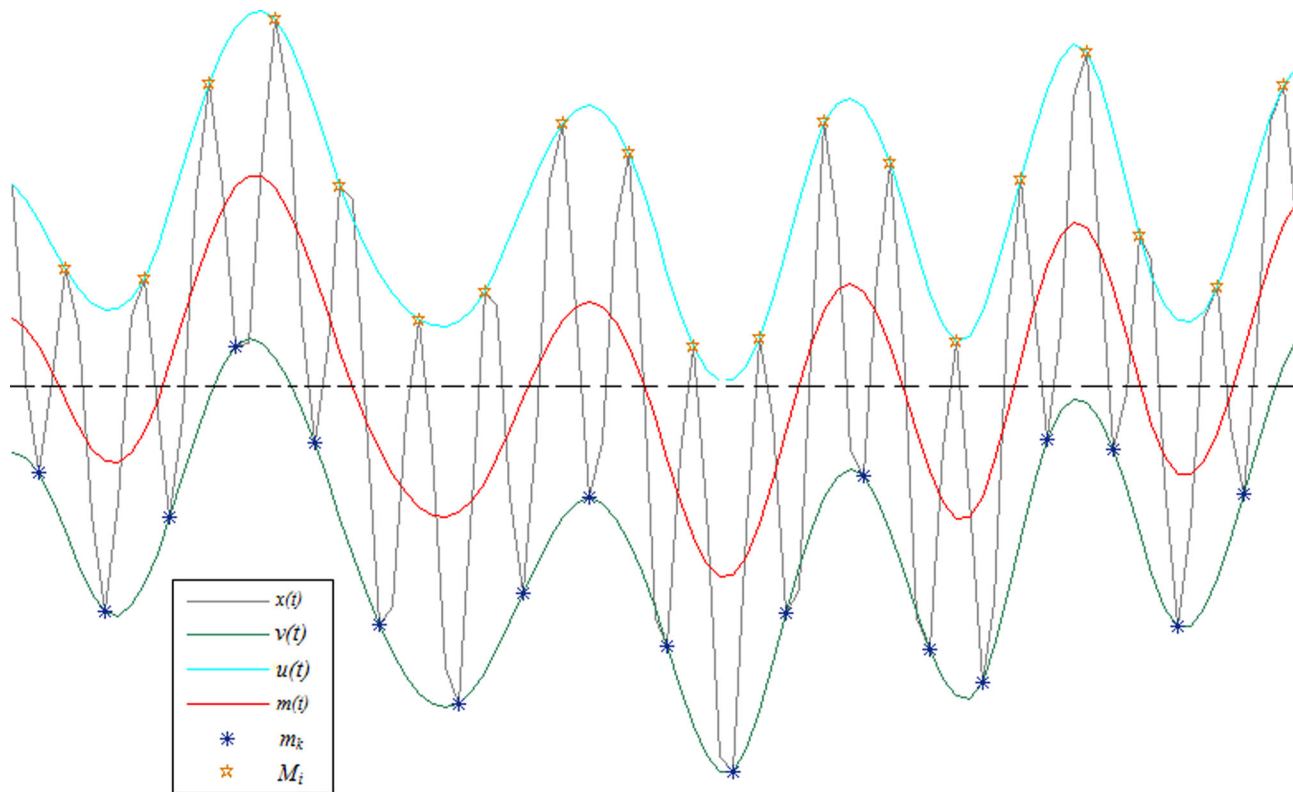


**Figure 1.** The mean spline. For a signal  $x(t)$ , the upper interpolating envelop  $u(t)$  is produced by the local maxima  $M_i$ . The lower interpolating envelop  $v(t)$  is produced by the minima  $m_k$ . The mean spline  $m(t)$  is produced by the upper envelope  $u(t)$  and the lower envelope  $v(t)$ . Subtract  $m(t)$  from  $x(t)$ , when res. is unchanged, the first IMF  $C_1(t)$  is obtained.

be unstable and lack the physical uniqueness. Wu & Huang (2009) proposed a new noise-assisted analysis method, called ensemble EMD (EEMD), to overcome the mode mixing problem. And, a complete EEMD (CEEMD) has recently been proposed by Torres *et al.* (2011). Wang *et al.* also compare the applications of EMD and EEMD on time–frequency analysis of seismic signal and find the time–frequency spectrum obtained by EEMD reflects the geological subsurface geology more accurately in the time–frequency analysis of seismic profiles (Wang *et al.* 2012). However, if narrowband sub-signals that resulted from EEMD/CEEMD have some bandwidth, such as a Ricker wavelet or Morlet wavelet, the EEMD/CEEMD method will seek to collapse this to a single frequency (Han & van der Baan 2013). This can be interpreted as super-resolution, because it can help to analyse subtle changes, but it may mask the true bandwidth of the subsignals. In addition, this may not be suitable for all signal analysis, for example, if an attenuation analysis is required using spectral ratios (Reine *et al.* 2009, 2012a,b; Han & van der Baan 2013), and our studies are the same situation. Because only one appropriate IMF section is needed, we request this section include greater bandwidth. So, in such situation, EMD may provide better effect than EEMD/CEEMD. EMD is used as an adaptive data-driven filter. The spectrum from the proposed method is calculated by TK operator. The IMF, which is a narrow-band signal, guarantees the correct extraction of instantaneous attributes by using TK operator. The correctness is also confirmed by the model test and the well log information. In our applications, we can check whether the attributes obtained by the EMD/TK method are reasonable based on the model established by the actual seismic data and the logging parameters.

## 2.2 ESA

TK operator is a non-linear quadratic signal operator, which has been proposed based on Newton's law of motion as a method to compute IF totally using differentiations. The superb localization property, which is the distinct advantage of the energy operator, is the result of the differentiation-based method. It involves at most five neighbouring data points to evaluate the frequency at the central point. It does not involve the integral transforms, which HT or Fourier transform involves. The TK operator also exhibits several other attractive properties such as simplicity, efficiency and ability to track instantaneously varying special patterns (Hamila *et al.* 2000).

The idea is based on a signal having the following form:

$$x(t) = a \cos \omega t, \quad (4)$$

then, an energy operator  $\psi$  is defined as

$$\psi(x) = [\dot{x}(t)]^2 - x(t)\ddot{x}(t), \quad (5)$$

where  $\dot{x}(t)$  represents first derivatives of  $x(t)$  and  $\ddot{x}(t)$  represents second derivatives of  $x(t)$  with respect to time. For the simple signal in eq.(4) with constant amplitude and frequency, we will have

$$\psi(x) = a^2(t)\omega^2(t), \quad (6)$$

and

$$\psi(\dot{x}) = a^2(t)\omega^4(t). \quad (7)$$

By simply manipulating with the eqs (6) and (7), we have

$$\omega = \sqrt{\frac{\psi(\dot{x})}{\psi(x)}} \quad \text{and} \quad a = \frac{\psi(x)}{\sqrt{\psi(\dot{x})}}. \quad (8)$$

From eq.(8) we can find the amplitude and frequency are determined by the  $\psi(x)$  and  $\psi(\dot{x})$ .

The TK energy operator approach is extended to the AM–FM signals whose, both, the amplitude and the frequency are functions of time by Kaiser (1990) and Maragos *et al.* (1993).

For a discrete AM–FM signal with time-varying amplitude  $a(n)$  and time-varying phase  $\varphi(n)$  has the following general expression:

$$x(n) = a(n) \cos [\varphi(n)]. \quad (9)$$

Define the non-linear signal operator  $\psi_d$  for formula (9):

$$\psi_d(x(n)) = x^2(n) - x(n-1)x(n+1). \quad (10)$$

The TK energy operator can be used to separate the monocomponent AM–FM signal  $x(n)$  into its IF signal  $\omega(n)$  and IA signal  $|a(n)|$  (Maragos *et al.* 1993). By the three-sample symmetric difference and computing, we obtain the IFs and IAs of the AM–FM signal (Maragos *et al.* 1993):

$$\omega(n) \approx \arccos [1 - \psi_d[x(n+1) - x(n-1)]/2\psi_d[x(n)]]/2, \quad (11)$$

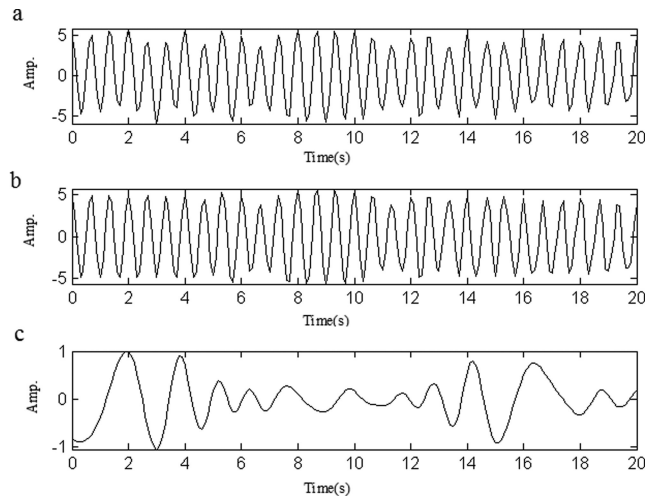


**Figure 2.** The simulated signal and its first two IMFs: (a) the simulated signal, (b) IMF1 and (c) IMF2.

$$|a(n)| \approx 2\psi_d[x(n)] / \sqrt{\psi_d[x(n+1) - x(n-1)]}. \quad (12)$$

For the AM–FM signals, we can find that the ESA method can offer only an approximation. The algorithm only works for mono-component functions, which can be seen from the very definition of the frequency and amplitude. Furthermore, when the amplitude is a time-varying function or the wave profiles have any intrawave modulations or harmonic distortions, the approximation produced by the ESA will be worsened and even break down (Huang *et al.* 2009).

Before an effective decomposition method is available, ESA method has been applied to the Fourier bandpassed signals only. The difficulty with the non-linear distorted waveform was not assessed at all. By using EMD to produce IMF, Huang *et al.* test TK operator on non-stationary and non-linear data for the first time (Huang *et al.* 2009). They found the method that combined the EMD and TK operator is a good solution to the very shortcomings and breakdown caused by non-linear waveform distortions, and EMD makes TK operator well suited for non-stationary signals analysis.

As an example, a simulated signal will be examined, given by the equation as

$$x(t) = 5\cos(\pi t/100)\cos(3\pi t) + \sin(\pi t^2/6),$$

where  $t \in [0, 20]$ .

EMD was applied to the simulated signal. After EMD process, IMF1 and IMF2 are generated (Fig. 2). Fig. 3 shows the IA and IF computed by the ESA to each IMF. Fig. 4 shows the IA and IF computed by the HT to each IMF. From Fig. 4 we can find there are the obvious end effects in HT. Since HT algorithm has inevitably window effects, the resulted instantaneous attributes have non-instantaneous response characteristics. As shown from Fig. 4, modulation will be generated at both ends of the resulted modulated signal and the intermediate portion of the mutations. The amplitude decays exponentially, so the demodulation error increases. Thus, ESA is superior to the HT algorithm.

### 2.3 EMD/TK as a spectral decomposition technology

Scattering and absorption can cause attenuation of seismic waves (Duchesne *et al.* 2011). Anderson & Hampton (1980a) found that scattering is the main mechanism for attenuation in gas-prone

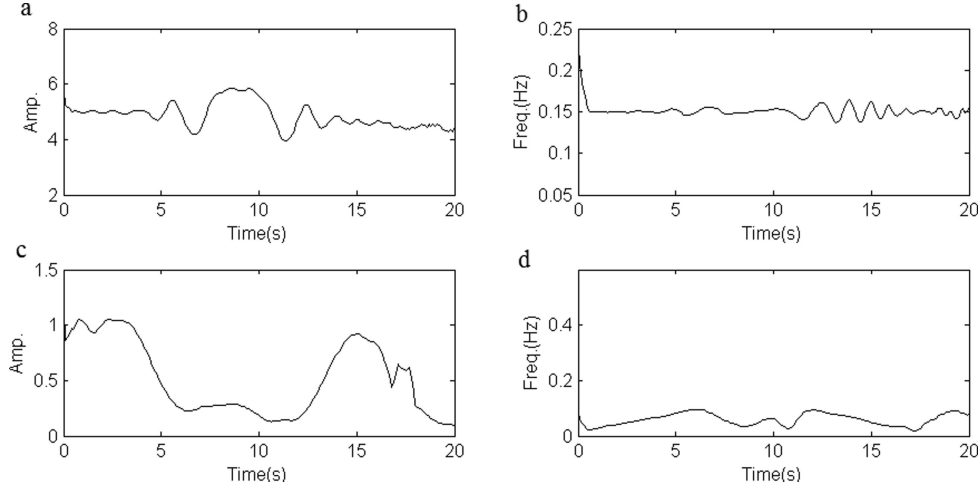


**Figure 3.** IAs and IFs of IMF1 and IMF2 using EMD/TK: (a) IA of IMF1, (b) IF of IMF1, (c) IA of IMF2 and (d) IF of IMF2.

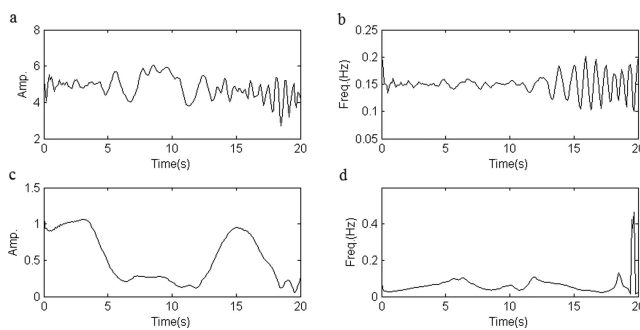


**Figure 4.** IAs and IFs of IMF1 and IMF2 using HT: (a) IA of IMF1, (b) IF of IMF1, (c) IA of IMF2 and (d) IF of IMF2.

geological media. Gas quantity and bubble size are the main factors to the attenuation in such geological media. A small quantity of gas (5 per cent or less) presented in porous media can dominate the acoustic characteristics of the sediments and increase reflection amplitude significantly, and the increase of the amount of gas in the reservoir (more than 5 per cent) does not cause the significant increase of seismic reflection amplitude (Domenico 1974; Anderson & Hampton 1980a). Bubble size is related to resonance frequency of gas bubbles, which is a function of the bubble radius (Anderson & Hampton 1980a). Below resonance frequency, near resonance frequency and above resonance frequency of the bubbles included in the gassy material are the three frequency regions that must be considered in scattering of a seismic wave (Anderson & Hampton 1980a,b). Below resonance frequency, scattering which is proportional to the fourth power of frequency is small. Near resonance frequency, scattering is a sharp maximum whereas above resonance frequency scattering, which is equal to four times the bubble physical cross-section, is constant.

Gas-prone sediments often exhibit low-frequency shadows (e.g. Castagna *et al.* 2003; Duchesne *et al.* 2011). However, until now, the nature of low-frequency shadows is still puzzling although low-frequency shadows are commonly used as hydrocarbon indicators for almost three decades (Taner *et al.* 1979; Castagna *et al.* 2003; Ebrom 2004; Duchesne *et al.* 2011). Two mechanisms are proposed by Taner *et al.* (1979) to explain the presence of low-frequency shadows. One is that higher frequency in gas-prone geological lay-

ers is filtered by the frequency-dependent absorption of gas. The other is that an inadequate summation of reflectors located right beneath the gas-prone geological layers is produced by the augmentation of the two-way traveltimes in these layers due to low seismic velocities of such material. However, Taner *et al.* (1979) judged the interpretation of some of their views was not enough such as low-frequency shadows associated with fracture zones in brittle rocks. At the 1996 SEG Summer Research Workshop, Dan Ebrom summarized at least 10 mechanisms to explain these low-frequency shadows. Other than intrinsic attenuation, Castagna *et al.* (2003) think that one or more of the following mechanisms for introducing low-frequency shadows may be at work at any given time: misstacking of locally converted shear waves and peg-leg multiples; improper moveout correction and loss of high frequencies upon stacking; normal moveout (NMO) stretch of far-offset information; and time-varying deconvolution processing adding a low-frequency tail to the wavelet.

As an effective technique for geological interpretations from seismic reflection data, spectral decomposition technique transforms seismic records from the time domain into a time–frequency space in which different localized frequency content is represented as a function of time, using the fact that different frequencies have different response characteristics among different scales of geological bodies to image geological features (e.g. Partyka *et al.* 1999). Thus, individual seismic volumes are transformed into multiple frequency volumes that preferentially enhance and maximize geophysical responses that appear within particular frequency bands (Puryear *et al.* 2012).

Since the seismic signal is a non-stationary and non-linear signal and the seismic signals also have multifrequency components, the above-mentioned ESA method alone is not effective when applied to seismic signals. Thus, we introduce the EMD combined ESA method to seismic signals and extend the EMD/TK algorithm as a spectral decomposition method for reservoir gas-containing detection.

The EMD method can decompose a multicomponent signal into a series of monocomponent AM–FM signals that have the characteristics of bandpass filters. Following this idea, the EMD method is first used to decompose multicomponent seismic signals into monocomponent AM–FM signals (IMFs) to meet the conditions of the ESA. Note that the hydrocarbon information of the seismic signals

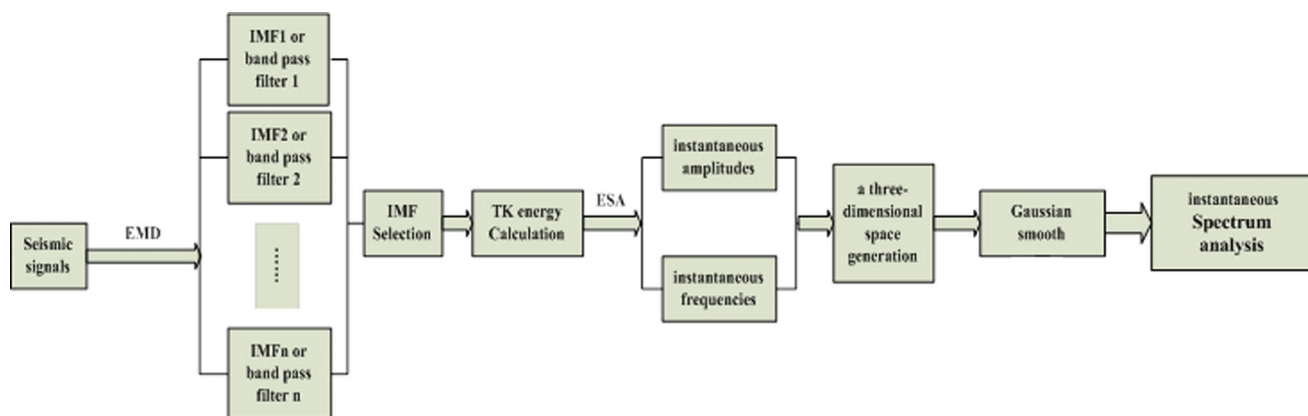


**Figure 5.** The flow chart of performing the TK energy separation algorithm after EMD. In the IMF selection, note that computing the correlation coefficient of each IMF and the seismic signal can help identify the main contributing component of the original signal. For a seismic section, however, it is time-consuming and unnecessary to compute the correlation coefficient for every seismic trace. We can extract a few seismic traces for correlation analysis, and the analysis results are applied to the whole seismic section. Then, combined with geological significance, we can choose the IMF seismic section that best reflects the reservoir characteristics of the original seismic section.

is embodied most in a certain frequency range. Therefore, after EMD process, the hydrocarbon information in the original seismic signals will be reflected in one or several IMF signals. Select the IMF signal that best reflects the hydrocarbon information. Then, the TK ESA is implemented for the selected IMF to calculate the IFs and IAs. Here, both the IFs and IAs are a function of time, so a 3-D space  $[t, \omega(t), a(t)]$  can be defined.

Let

$$H(\omega, t) = \operatorname{Re} \left\{ \sum_{i=1}^n a_i(t) e^{i \int \omega_i(t) dt} \right\},$$

where  $\operatorname{Re}$  takes the real part of the result, and  $n$  denotes the number of seismic traces. Then, the 3-D space is generalized by means of a function of two variables  $H(\omega, t)$  to three variables  $[t, \omega, H(\omega, t)]$ , where  $a(t) = H[\omega(t), t]$ . Thus, the joint time–frequency distribution of the seismic signal is obtained. For better identification of the featured components, Gaussian smoothing is used on the joint time–frequency distribution.

Spectral decomposition can be performed based on the joint time–frequency distribution. Thus, we can obtain the common frequency sections in different frequency ranges for more prominent oil and gas information extraction.

This method is described in Fig. 5.

### 3 MATERIALS

#### 3.1 Seismic data

The broad-band migrated stacked seismic data from a gas field at the Eastern Ordos Basin, China is collected for analysis. The gas field locates in northern Shaanxi slope zone. The structure, which mainly deposited a set of stable carbonate rocks formation, tends to be stable. The gas field is mainly composed of marine carbonate reservoirs. The field's major producing gas reservoir is distributed in the first and fourth sections of the Mawu section, Fm Majiagou, Ordovician. Reservoir space is formed by karstification pores, fractures and caves, which belong to typically low-porosity, low-permeability and low-abundance lithologic gas reservoir traps.

A large number of previous studies have shown that due to tectonic movement uplift in the late Caledonian period, carbonate rocks in the Lower Palaeozoic are exposed to surface and subjected

to weathering and denudation, erosion and chemical corrosion, leaching after the sea receded in Ordovician of the middle Palaeozoic. There are significant karst features in the top surface of Fm Majiagou, mainly as groove landscape (Gu *et al.* 2007; Hou *et al.* 2011). The results of microfacies analysis indicate that most of the limestones of the Majiagou Formation formed in open sea shelf environments and tidal flat environments, and part of them was related to the development of reefs (Bao & Yang 2000).

Here, we mainly study the fourth section of the Mawu section. The fourth section's porosity ranges from 0.22 to 15.91 per cent, with an average porosity of approximately 4 per cent. The average permeability is  $1.518 \times 10^{-3} \mu\text{m}^2$ . The lithology in the reservoir segment is mainly brownish grey cavernous dolomite or shallow grey crystal powder dolomite. Its cover is low-speed Carboniferous clastic rocks strata, and high-speed compacted massive limestone locates in the bottom plate. Moderate-to-strong reflection amplitudes are formed on the seismic sections. Lateral distribution is stable. Therefore, the strong wave impedance difference in the study area is primarily caused by reservoir section. When the reservoir is gas-bearing, seismic reflection amplitude is stronger due to a greater difference from the wave impedances of the upper and lower surrounding rocks.

The broad-band migrated stacked seismic section of the target layer is illustrated in Fig. 6 (the 1.5–2.1 s slice in Inline77), which shows the study area is a relatively simple structure. Weak amplitude belt exists under the key horizon (black line) and it may be the response to the weathering crust. The key horizon interface is not only a geological era, but also a physical interface. The Inline77 section from the original seismic volume intersects a known prolific gas well A. The open flow capacity of well A is  $34.9133 \times 10^4 \text{ m}^3 \text{ d}^{-1}$ . At first, we use this section to examine the effects of the EMD/TK.

**Table 1.** Rock properties for geological model. Note that  $\zeta$  is diffusion coefficient.  $\eta$  is viscous coefficient.

Layer number	$V_p$ ( $\text{m} \cdot \text{s}^{-1}$ )	$\rho$ ( $\text{g} \cdot \text{cm}^{-3}$ )	$\zeta$ (Hz)	$\eta$ ( $\text{m}^2 \cdot \text{s}^{-1}$ )	$Q$
①	4300	1.2	1.0	1.0	200
②	4500	1.25	1.0	1.0	200
③	4600	1.3	1.0	1.0	200
④	4400	1.2	10	500	5
⑤	4700	1.35	1.0	1.0	200
⑥	4800	1.4	1.0	1.0	200

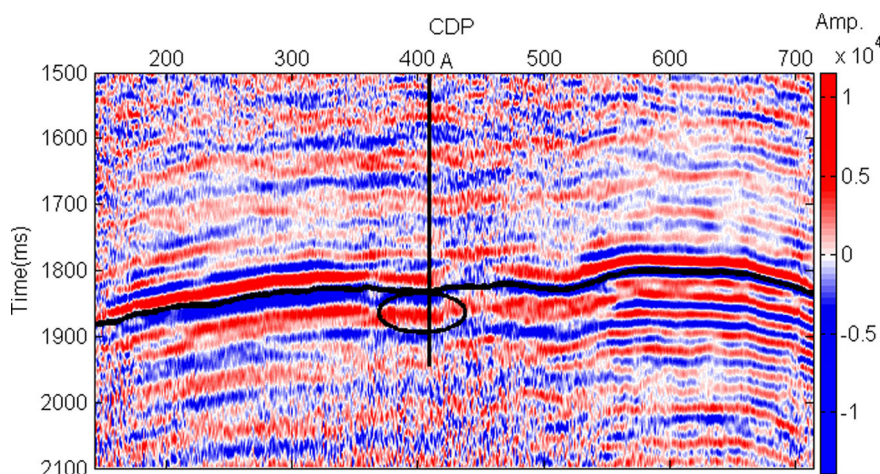


**Figure 6.** The original seismic section.

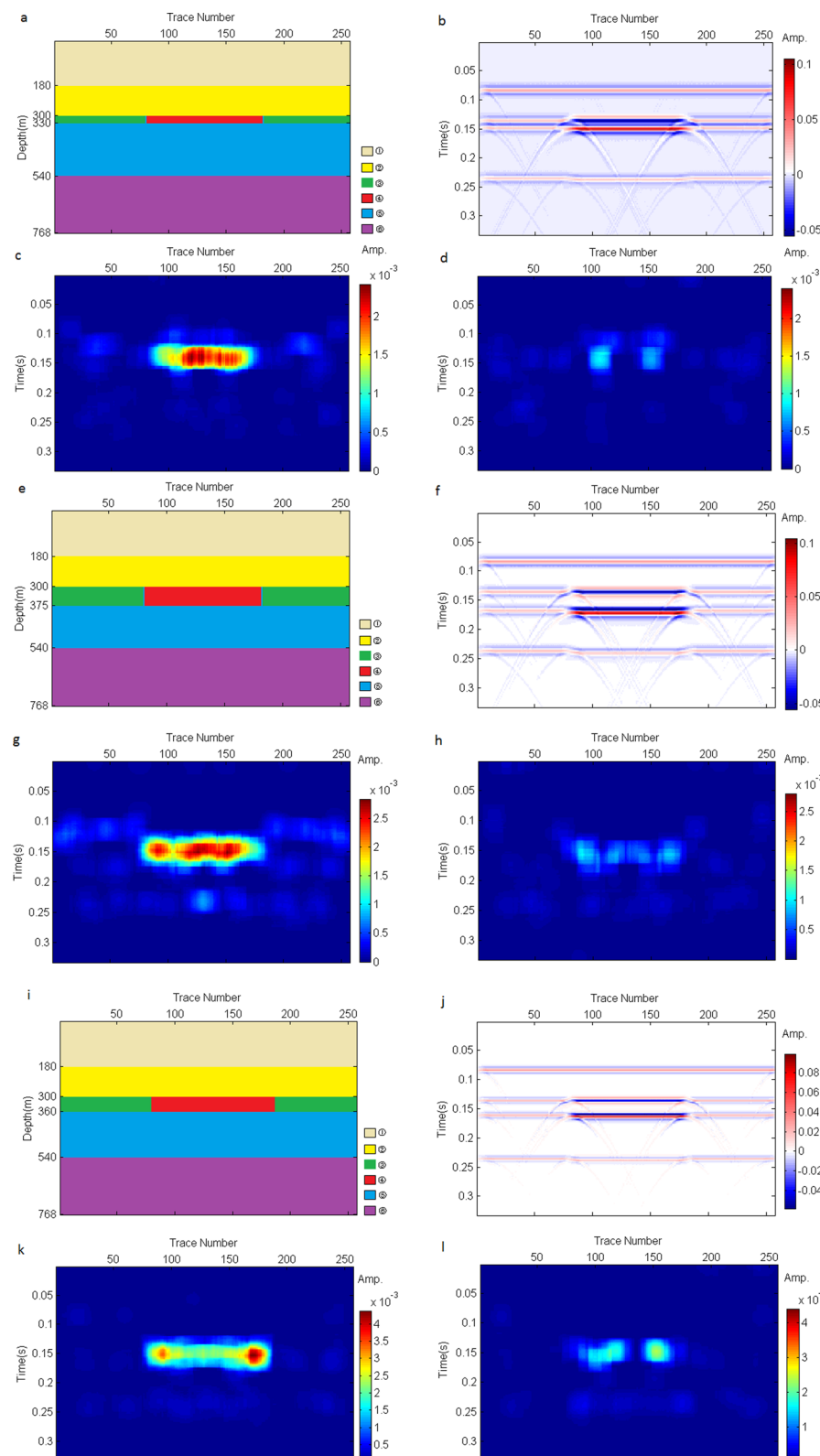


**Figure 7.** Seismic response and instantaneous spectral decomposition of models: (a) the geological model 1; (b) seismic response of the geological model 1; (c) common frequency section at low frequency for model 1; (d) common frequency section at high frequency for model 1; (e) the geological model 2; (f) seismic response of the geological model 2; (g) common frequency section at low frequency for model 2; (h) common frequency section at high frequency for model 2; (i) the geological model 3; (j) seismic response of the geological model 3; (k) common frequency section at low frequency for model 3 and (l) common frequency section at high frequency for model 3.

Reservoir is beneath the key horizon. Study area is set by a black ellipse, where the typical prolific gas well A is located and good gas production is obtained. The seismic signals are sampled at 1 ms. Three seismic traces are first extracted from the original seismic section for analysis.

Then, the method is used to the 3-D seismic data. There are three gas-producing wells (A, B and C) in the object area. The open flow capacity of well B is  $25 \times 10^4 \text{ m}^3 \text{ d}^{-1}$ , and the open flow capacity of well C is  $46.6567 \times 10^4 \text{ m}^3 \text{ d}^{-1}$ . C is the most prolific gas well. A is the less prolific gas well and B is relatively a minimal rich gas wells.

### 3.2 Model test

To validate the effectiveness of the EMD/TK method for hydrocarbon detection and further test the EMD/TK method validation in the gas field located in the eastern Ordos Basin, China, we produce the various models to simulate the seismic response based on the diffusive-viscous wave equation (Korneev *et al.* 2004).

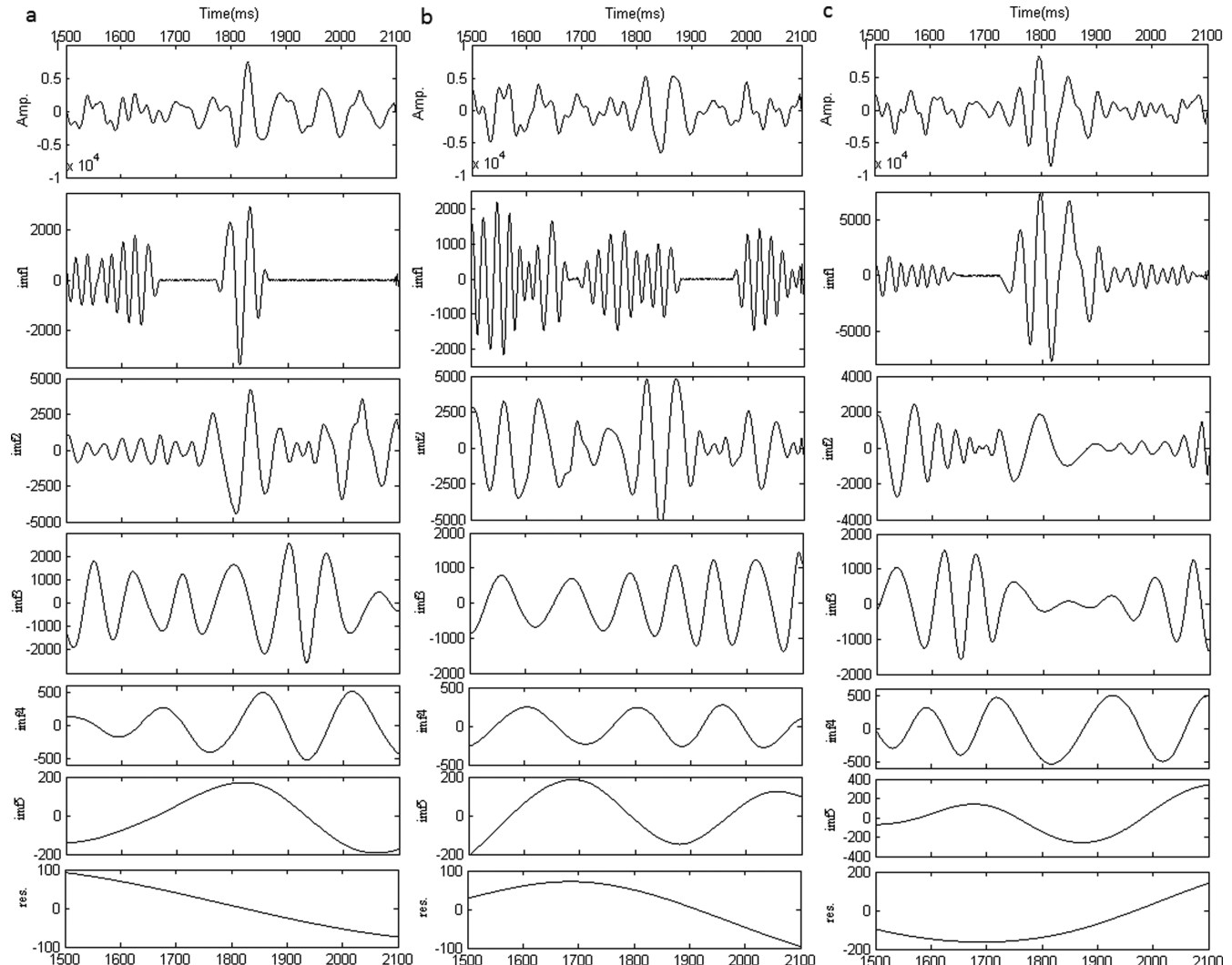


**Figure 8.** The EMD method applied to the three seismic traces. Among them, the seismic trace at CDP409 passes through well A. The vertical axis is amplitude: (a) shows the seismic trace at CDP242 and its EMD decomposition results; (b) shows the seismic trace at CDP409 and its EMD decomposition results; (c) shows the seismic trace at CDP542 and its EMD decomposition results. Res. denotes the margin of the seismic trace.

The geological models include six formations. The parameters of each layer are shown in Table 1 (Xue *et al.* 2013a). The layer marked ③ is the dry layer (excluding gas). The layer marked ④ is the gas-bearing layer. Sampling frequency is 512 Hz. Three models are designed with the different thickness of the gas-bearing layer ④ and the frequency of the wavelet.

In model 1, the thickness of the gas-bearing layer ④ is 30 m. The frequency of the wavelet is 40 Hz. In model 2, the thickness of the gas-bearing layer ④ is changed to 75 m. The frequency of the wavelet is 40 Hz. In model 3, the thickness of the gas-bearing layer ④ is changed to 60 m. The frequency of the wavelet is changed to 60 Hz. The geological models and their corresponding seismic responses are, respectively, shown in Fig. 7.

## 4. RESULTS AND DISCUSSION

### 4.1. Results

The results of using EMD/TK to models are shown in Figs 7(c, d, g, h, k and l). The three seismic traces and their EMD results are

**Table 2.** Correlation analysis of the three seismic traces and their six corresponding IMFs. The correlation coefficients of the seismic trace at CDP242 and its six IMF signals (imf1–imf6), the seismic trace at CDP409 and its six IMF signals (imf1–imf6) and the seismic trace at CDP542 and its six IMF signals (imf1–imf6) are given.

	imf1	imf2	imf3	imf4	imf5	imf6
CDP242	0.5065	0.7457	0.5035	0.0153	0.0291	-0.0238
CDP409	0.3569	0.8911	0.3049	-0.0208	-0.0106	-0.0063
CDP542	0.8818	0.3	0.1944	0.0648	0.0383	0.04

shown in Figs 8(a)–(c). Correlation analysis of the three seismic traces and their six IMFs is shown in Table 2. Take the IMF2 of CDP409 seismic trace for example, Figs 9(a) and (b) show the IA and IF computed by the HT to the IMF2 of CDP409 seismic trace. Figs 9(c) and (d) show the IA and IF computed by the ESA to the IMF2 of CDP409 seismic trace. From the enlarged part figures in Figs 9(a) and (c), the obvious end effects in IAs can be found in HT. In Figs 9(b) and (d), the end effects in IFs are more clear in HT than those in ESA. The instantaneous attributes resulted from HT show the non-instantaneous response characteristics due to window effects. ESA shows a better instantaneously adapting nature in both the endpoint segments and the middle segments in IAs and IFs. The comparison of the IAs and IFs computed by the ESA and HT, respectively, also shows ESA is superior to the HT algorithm for the seismic signal.

Then, the EMD method is used for the original seismic section. The resultant first three IMFs are shown in Figs 10(a)–(c). Fig. 11 is the time–frequency spectrum of the IMF2 seismic section using the EMD/TK method. Fig. 12 shows the 14–18 Hz (Fig. 12a) and 26–30 Hz (Fig. 12b) common frequency sections corresponding to the IMF2 section in Fig. 10(b). Finally, Fig. 13 gives the three seismic traces interesting wells A, B and C and their corresponding time–frequency spectrum based on EMD/TK. The common frequency slices of the fourth section of the Mawu section in the gas field are shown in Fig. 14.

## 4.2 Data analysis

### 4.2.1 Model analysis

As can be seen from Fig. 7, the gas-bearing reservoir has larger energy (Figs 7c, d, g, h, k and l). In the common frequency section at low frequency (Figs 7c, g and k), we can see a strong energy in the reservoir. However, in the common frequency section at high frequency (Figs 7d, h and l), the reservoir energy is weakened.

The frequency of model 1 is close to the dominant frequency of the actual seismic signal in the region. The thickness of model 1 is near the real thickness in the region. Model 1 shows EMD/TK method can be applied to the seismic data in the gas field.

Models 2 and 3 are the case to demonstrate that the frequency of the wavelet and the thickness of the gas-bearing layer and the thickness of formations below the gas-bearing layer are changed, EMD/TK method can still detect the gas-bearing reservoir well.

### 4.2.2 IMF selection

From Fig. 8, we find that there are six IMF components for each seismic trace after EMD decomposition. For the three seismic traces, from Table 1 we can find a strong correlation exists in the first to third IMFs. We consider the first to third IMFs to be the main contributors to each seismic trace. Therefore, following the analysis of the whole seismic section, we analysed only the first three IMF components produced by the original seismic section.

For the original seismic section, as analysed above, we only consider the first three IMFs. There is little difference between the object area and its surroundings in the original seismic section in Fig. 6. The first IMF signal (IMF1) shown in Fig. 10(a) is extracted first. The seismic information with smaller and larger common depth points (CDPs) is embodied in IMF1, which can also be observed in Table 2. The correlation coefficient of IMF1 and the original seismic section at CDP242 and CDP542 are larger than at CDP409. The correlation coefficient of IMF2 and the original seismic section at CDP409 are the largest. Therefore, the gas information in this section is less reflected. Fig. 10(b) shows the second IMF signal (IMF2) of the original seismic section. We can see that the second

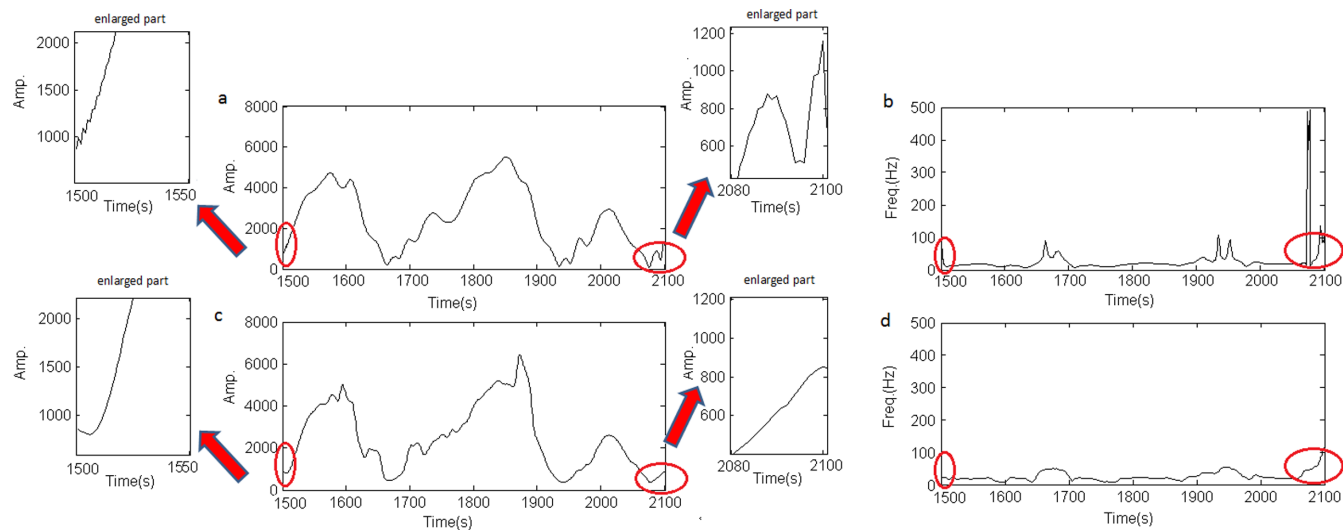


**Figure 9.** HT and ESA applied to IMF2 of CDP409, respectively: (a) shows the IA computed by the HT to IMF2 of CDP409 seismic trace; (b) shows the IF computed by the HT to IMF2 of CDP409 seismic trace; (c) shows the IA computed by the ESA to IMF2 of CDP409 seismic trace and (d) shows the IF computed by the ESA to IMF2 of CDP409 seismic trace.

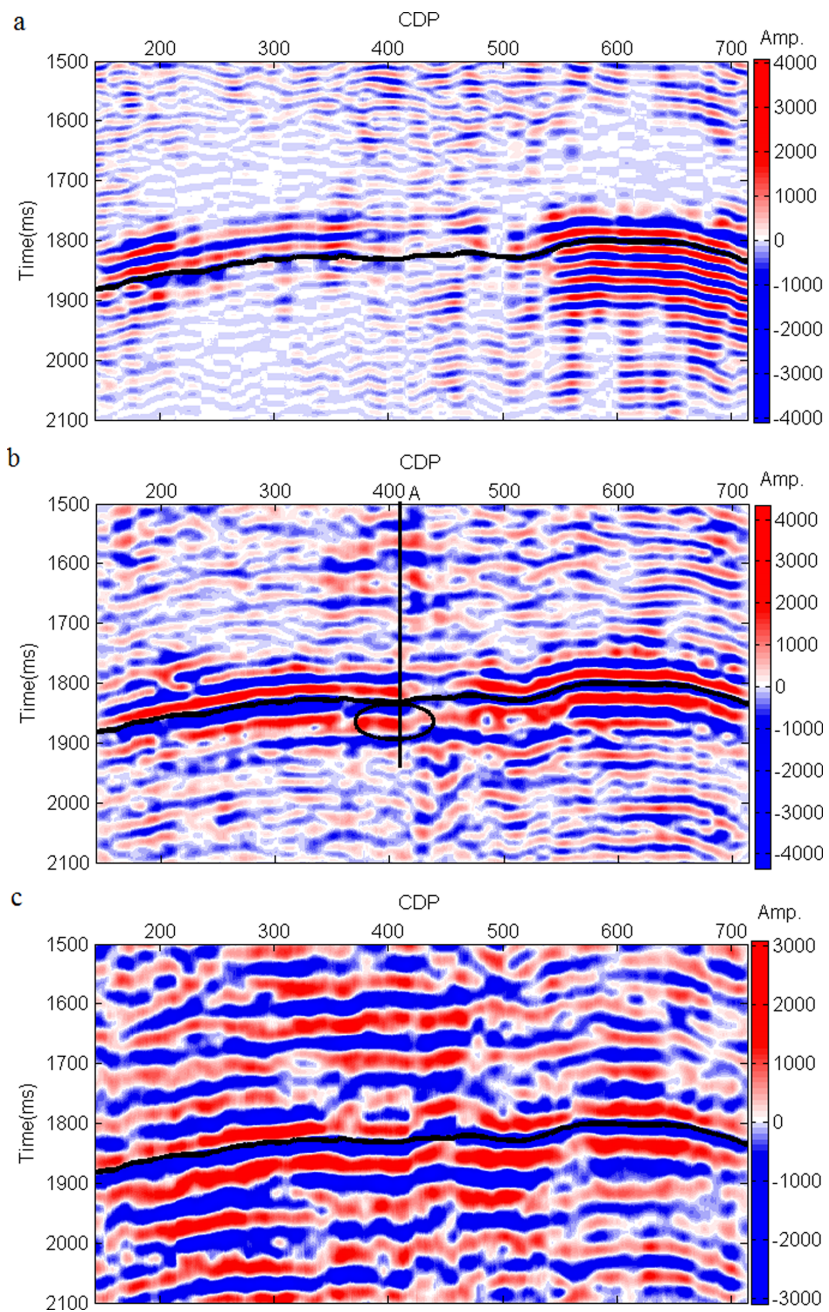


**Figure 10.** The first three components of the original seismic section: IMF1 (a), IMF2 (b) and IMF3 (c).

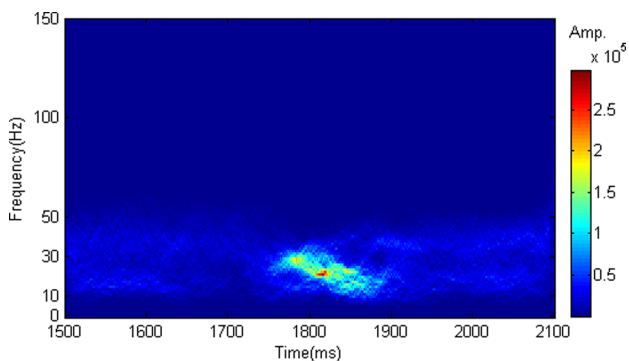


**Figure 11.** The time–frequency spectrum of the IMF2 seismic section.

IMF signal (IMF2) of the original seismic section contains less interference compared with the original seismic section. The position of the object area and the difference between the object area and its surroundings are distinct. The details of the original seismic section are greater and are enhanced in the IMF2 seismic section, which may reveal the details of the gas information. The gas information is mainly reflected in this frequency range. Due to its larger scale, the main reflector becomes increasingly blurred in the third IMF (IMF3), and its reflected energy is weaker (Fig. 10c). Therefore, we select the second IMF signal (IMF2) for further processing.

Note that each IMF has different frequency components, potentially highlighting different geological and stratigraphic information. Here, EMD is used as an adaptive data-driven filter to provide a narrow band signal for meeting the TK operator's requirement. The selected IMF2 section is considered as an appropriate filter of

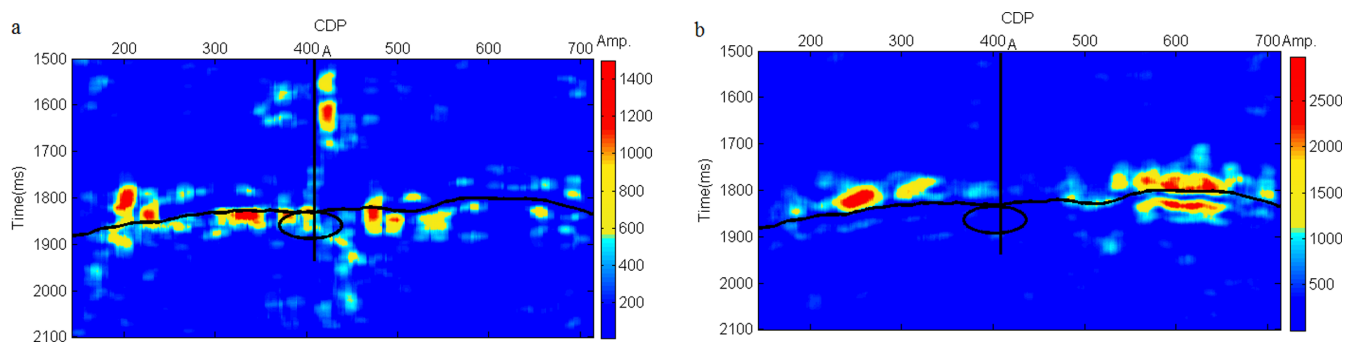


**Figure 12.** Comparative analysis of common frequency section corresponding to the IMF2 section in Fig. 10(b). (a) The 14–18 Hz common frequency section and (b) the 26–30 Hz common frequency section.

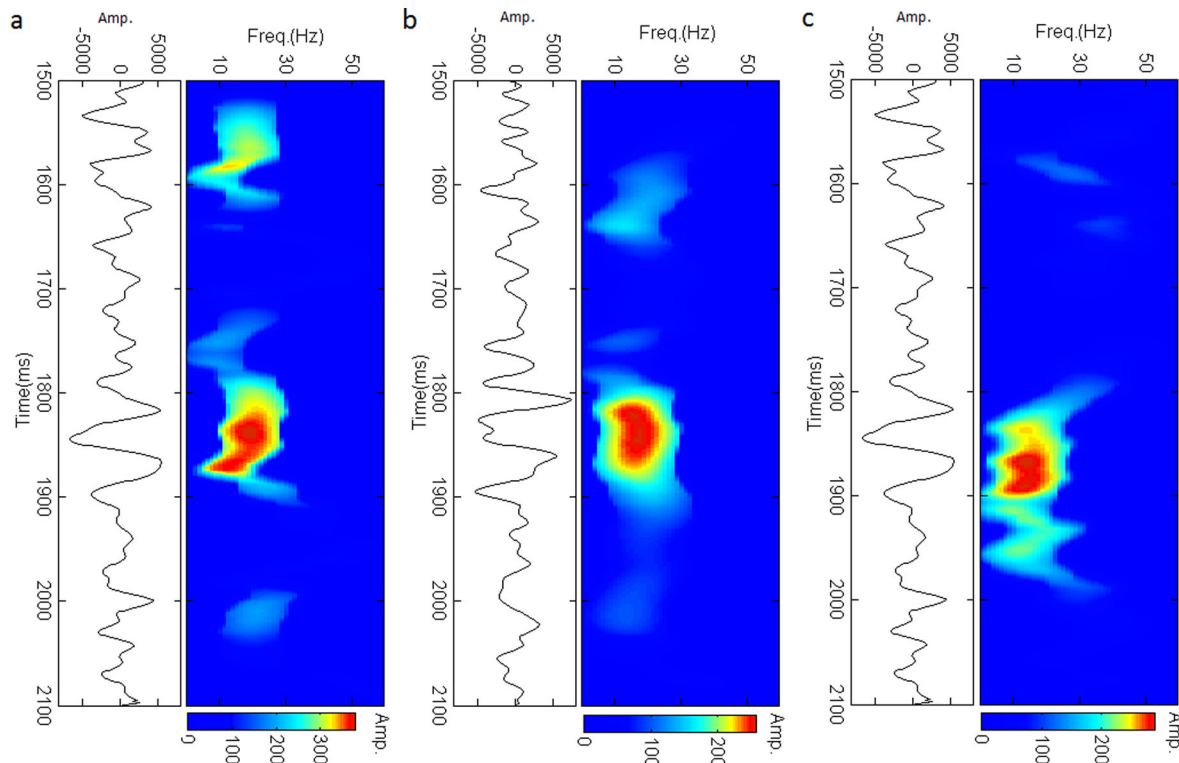


**Figure 13.** Three seismic traces intersecting well A, B and C and their corresponding time–frequency spectrum based on EMD/TK: (a) The seismic trace intersecting well A and its corresponding time–frequency spectrum; (b) the seismic trace intersecting well B and its corresponding time–frequency spectrum; (c) the seismic trace intersecting well C and its corresponding time–frequency spectrum. Note that here we only use the IMF2 of each seismic traces to generate the corresponding time–frequency spectrum based on EMD/TK.

the original seismic section. The EMD process can also be considered to be a principal component analysis here. For hydrocarbon detection, we only study the method which can more prominently explain the characteristics of oil and gas. The whole picture or information of the original seismic data sometimes is not required. The reason for only using one appropriate IMF (in most cases, for field data, the choice is the higher frequencies components) section for hydrocarbon detection is that the higher frequencies components of the original seismic section will reflect the fine information. The volume and mass ratio of oil and gas in reservoir to the whole reservoir rocks are very low. Furthermore, the oil and gas which filled in the pores of the rock matrix are deeply buried in reservoirs. Due to the strong heterogeneity, the porous fluid seismic response is weak and it is difficult for hydrocarbon detections. Weak variations or differences in porous fluid seismic response will be reflected in the fine information of the original seismic section. So we usually

select the higher frequencies components (such as IMF2) for analysis. The lower frequencies components (such as IMF3, IMF4 and the others), we think, reflect the coarse information of the original seismic section, such as mainly the formation information. In our current process, for hydrocarbon detection, only one appropriate IMF section is needed. And, its effect can be confirmed by the well log information and the model test. This are also the traditional practices in the exploration field for testing whether a method is valid for one area. The difference of the IMF selection in seismic sections intersecting gas-bearing well and water-bearing well can also be found in Xue *et al.* (2013b).

#### 4.2.3 Hydrocarbon detection

From the time–frequency spectrum of the IMF2 seismic section (Fig. 11), we find that the dominant frequency range is 12–30 Hz.

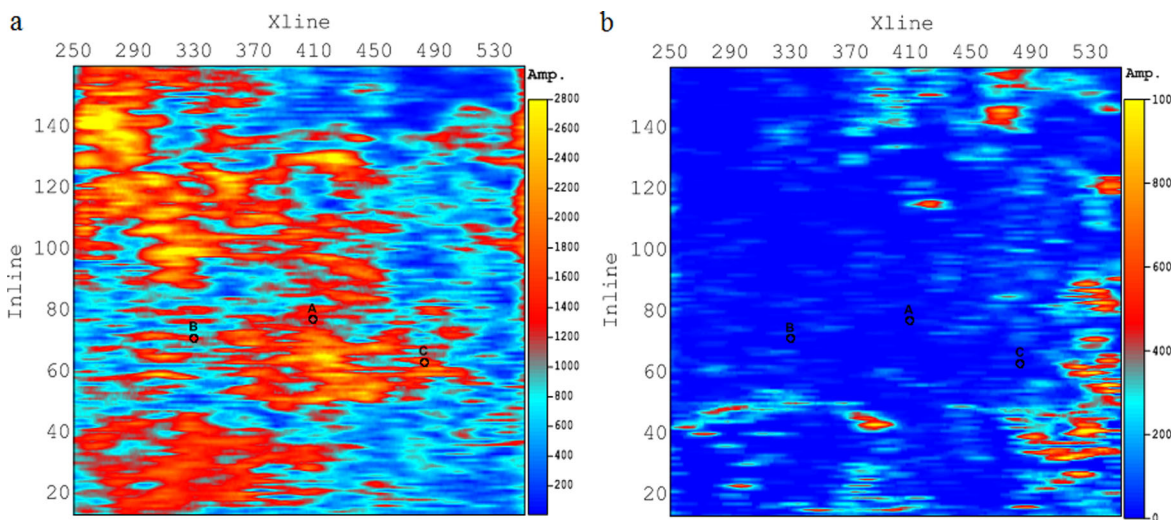


**Figure 14.** The common frequency slices of the fourth section of the Mawu section in the gas field: (a) the 14–18 Hz common frequency slices and (b) the 26–30 Hz common frequency slices.

In the known oil- and gas-bearing section, the visible characteristics of the high-energy distribution are obvious.

In Fig. 12(a), we find a strong energy distribution within the detection area (black ellipse). In the 26–30 Hz common frequency section (Fig. 12b), the energy is fully absorbed in the detection area (black ellipse). These instantaneous spectrums show the obvious characteristics of the attenuation of high-frequency energy and the enhancement of low-frequency energy and indicate that the EMD/TK method can provide a good statistical interpretation.

Comparing with the other methods (Appendix), we think the EMD/TK method is effective in oil and gas detection. The EMD/TK method only analyses the seismic section containing the oil and gas information most within a certain frequency range rather than the whole seismic section. The time resolution and the frequency resolution are higher, and the method can give a good statistical interpretation.

For the gas reservoir, higher frequencies are more rapidly attenuated compared to lower frequencies. Therefore, the common frequency section at low frequency corresponding to the high amplitudes and the common frequency section at high frequency corresponding to the weak amplitudes indicate the favourable gas reservoir distribution area. Fig. 13 shows the corresponding time–frequency spectrums based on EMD/TK of the three seismic traces intersecting well A, B and C. Particularly, the strong red energy in the three time–frequency spectrums correspond to the reservoir location of these three gas wells. Fig. 13 shows that the capability of the EMD/TK method to track the time–frequency energy locating the main seismic events in the trace. In Fig. 14(a), the three measured gas wells are within the position of the strong amplitudes. In Fig. 14(b), the location of the three measured gas wells are within the weak amplitudes. Comparing these two figures, the distribution of favourable reservoirs is within the region of high amplitudes at the low frequencies and weak amplitudes at the high frequencies. A better preliminary evaluation of reservoir gas-bearing detection can be given by the EMD/TK method.

## 5 CONCLUSION

The question of how to obtain a joint time–frequency representation using the EMD method and the TK ESA for seismic signals is

discussed in this paper. For the proposed method, the TK ESA is used to estimate the IF and amplitude of seismic signals. The EMD method is used as a multiband filter to decompose the original seismic signals into the components in the temporal domain. The EMD method is well-adapted to non-stationary signals, and the TK ESA can provide a good estimate of the IF and the IA. The instantaneous spectrums of the EMD/TK method have certain oil and gas detection capabilities. The models and the application in the eastern area of the Ordos Basin show the effectiveness of the EMD/TK method for hydrocarbon detection. The EMD/TK method provides spectral information at a level of detail not available with conventional spectral decomposition methods and offers new domains for processing and interpreting seismic reflection data.

## ACKNOWLEDGEMENTS

This study was supported by National Natural Science Foundation of China (Grant Nos. 41274128, 40930424 and 41304080), which is greatly appreciated. This work was made possible by support and cooperation from the Cultivating programme of the excellent innovation team of Chengdu University of Technology. The authors are grateful to the anonymous reviewers for their constructive comments. Special thanks also go to the Editor-in-Chief for his interest in this work and comments.

## REFERENCES

- Anderson, A.L. & Hampton, L.D., 1980a. Acoustics of gas-bearing sediments I: background, *J. acoust. Soc. Am.*, **67**(6), 1865–1889.
- Anderson, A.L. & Hampton, L.D., 1980b. Acoustics of gas-bearing sediments II: measurements and models, *J. acoust. Soc. Am.*, **67**(6), 1890–1903.
- Bao, H. & Yang, C., 2000. Study on microfacies of Majiagou formation, lower Ordovician, Eastern Ordos, North China, *J. Palaeogeogr.*, **2**, 31–42.
- Battista, B.M., Knapp, C., McGee, T. & Goebel, V., 2007. Application of the empirical mode decomposition and Hilbert-Huang transform to seismic reflection data, *Geophysics*, **72**, H29–H37.
- Bedrosian, E., 1963. On the quadrature approximation to the Hilbert transform of modulated signals, *Proc. IEEE*, **51**, 868–869.
- Castagna, J.P., Sun, S. & Siegfried, R.W., 2003. Instantaneous spectral analysis: detection of low-frequency shadows associated with hydrocarbons, *Leading Edge*, **22**, 120–127.

- Chakraborty, A. & Okaya, D., 1995. Frequency-time decomposition of seismic data using wavelet-based methods, *Geophysics*, **60**, 1906–1916.
- de Matos, M.C. & Johann, P.R., 2007. Revealing geological features through seismic attributes extracted from the wavelet transform Teager-Kaiser energy, in *Proceedings of 2007 SEG Annual Meeting, San Antonio, Texas*.
- de Matos, M.C., Marfurt, K.J., Johann, P. & Adolfo, J., 2008. Brazilian deep water carbonate reservoir study using the Wavelet Transform Teager-Kaiser Energy, in *SEG Technical Program Expanded Abstracts*, pp. 1516–1520.
- de Matos, M.C., Marfurt, K.J., Johann, P.R.S., Rosseto, J.A., Lourenço, A.T.A. & Diniz, J.L., 2009. Wavelet transform Teager-Kaiser energy applied to a carbonate field in Brazil, *Leading Edge*, **28**, 708–713.
- Domenico, S.N., 1974. Effect of water saturation on seismic reflectivity of sand reservoirs encased in shale, *Geophysics*, **39**(6), 759–769.
- Duchesne, M. J., Halliday, E. J. & Barrie, J. V., 2011. Analyzing seismic imagery in the time-amplitude and time-frequency domains to determine fluid nature and migration pathways: a case study from the Queen Charlotte Basin, offshore British Columbia, *J. appl. Geophys.*, **73**(2), 111–120.
- Ebrom, D., 2004. The low-frequency gas shadow on seismic sections, *Leading Edge*, **23**(8), 772, doi:10.1190/1.1786898.
- Ehrhardt, M., Villinger, H. & Schiffler, S., 2012. Evaluation of decomposition tools for sea floor pressure data: a practical comparison of modern and classical approaches, *Comput. Geosci.*, **45**, 4–12.
- Flandrin, P., Rilling, G. & Goncalves, P., 2004. Empirical mode decomposition as a filter bank, *IEEE Signal Process. Lett.*, **11**, 112–114.
- Gu, D.-h., Dai, J.-y., Lan, C.-l. & He, S.-l., 2007. High-precision integrative recognition technology for flutings in Jingbian Gasfield, Ordos Basin, *Petrol. Explor. Dev.*, **34**, 60–64 (in Chinese).
- Hamila, R., Renfors, M., Haverinen, T. & Gunnarsson, G., 2000. Teager-kaiser operator based filtering, in *Proceedings of EUPSICO 2000: European Signal Processing Conference, Tampere, Finland*, pp. 1545–1548.
- Han, J. & van der Baan, M., 2013. Empirical mode decomposition for seismic time-frequency analysis, *Geophysics*, **78**, O9–O19.
- Hassan, H.H., 2005. Empirical mode decomposition (EMD) of potential field data: airborne gravity data as an example, in *Proceedings of 2005 SEG Annual Meeting, Houston, Texas*, pp. 704–706.
- Hou, F., Fang, S. & He, J. et al., 2011. Distribution characters and comprehensive evaluation of middle Ordovician Majiagou 51–54 submembers reservoirs in Jingbian Gas field Area, Ordos Basin, *Mar. Origin Petrol. Geol.*, **16**, 1–13 (in Chinese).
- Huang, N.E. & Shen, S.S., 2005. *Hilbert-Huang Transform and Its Applications*, Vol. 5, World Scientific Press.
- Huang, N.E. & Wu, Z., 2008. A review on Hilbert-Huang transform: method and its applications to geophysical studies, *Rev. Geophys.*, **46**, RG2006, doi:10.1029/2007RG000228.
- Huang, N.E. et al., 1998. The empirical mode decomposition and the Hilbert spectrum for nonlinear and non-stationary time series analysis, *Proc. R. Soc. A: Math. Phys. Eng. Sci.*, **454**, 903–995.
- Huang, N.E., Wu, Z., Long, S.R., Arnold, K.C., CHEN, X. & Blank, K., 2009. On instantaneous frequency, *Adv. Adapt. Data Anal.*, **1**, 177–229.
- Huang, Y.-P., Geng, J.-H., Zhong, G.-F., Guo, T.-L., Pu, Y., Ding, K.-Y. & Ma, J.-Q., 2011. Seismic attribute extraction based on HHT and its application in a marine carbonate area, *Appl. Geophys.*, **8**, 125–133.
- Kaiser, J.F., 1990. On Teager's energy algorithm and its generalization to continuous signals, in *Proceedings of Fourth IEEE Digital Signal Processing Workshop, Mohonk, New York*, 230 pp.
- Korneev, V.A., Goloshubin, G.M., Daley, T.M. & Silin, D.B., 2004. Seismic low-frequency effects in monitoring fluid-saturated reservoirs, *Geophysics*, **69**, 522–532.
- Macelloni, L., Battista, B.M. & Knapp, C.C., 2011. Optimal filtering high-resolution seismic reflection data using a weighted-mode empirical mode decomposition operator, *J. appl. Geophys.*, **75**, 603–614.
- Magrin-Chagnolleau, I. & Baranik, R.G., 1999. Empirical mode decomposition based frequency attributes, in *Proceedings of 1999 SEG Annual Meeting, Houston, Texas*.
- Maragos, P., Kaiser, J.F. & Quatieri, T.F., 1993. On amplitude and frequency demodulation using energy operators, *IEEE Trans. Signal Process.*, **41**, 1532–1550.
- Nuttall, A.H., 1966. On the quadrature approximation to the Hilbert transform of modulated signals, *Proc. IEEE*, **54**, 1458–1459.
- Nuttall, A. & Bedrosian, E., 1966. On the quadrature approximation to the Hilbert transform of modulated signals, *Proc. IEEE*, **54**, 1458–1459.
- Partyka, G., Gridley, J. & Lopez, J., 1999. Interpretational applications of spectral decomposition in reservoir characterization, *Leading Edge*, **18**(3), 353–360.
- Potamianos, A. & Maragos, P., 1994. A comparison of the energy operator and the Hilbert transform approach to signal and speech demodulation, *Sign. Process.*, **37**, 95–120.
- Pureyear, C.I., Portniaguine, O.N., Cobos, C.M. & Castagna, J.P., 2012. Constrained least-squares spectral analysis: application to seismic data, *Geophysics*, **77**(5), V143–V167.
- Rato, R., Ortigueira, M. & Batista, A., 2008. On the HHT, its problems, and some solutions, *Mech. Syst. Signal Process.*, **22**, 1374–1394.
- Reine, C., Baan, M.v.d. & Clark, R., 2009. The robustness of seismic attenuation measurements using fixed- and variable-window time-frequency transforms, *Geophysics*, **74**, WA123–WA135.
- Reine, C., Clark, R. & van der Baan, M., 2012a. Robust prestack Q-determination using surface seismic data: part 1—method and synthetic examples, *Geophysics*, **77**, R45–R56.
- Reine, C., Clark, R. & van der Baan, M., 2012b. Robust prestack Q-determination using surface seismic data: part 2—3D case study, *Geophysics*, **77**, B1–B10.
- Sinha, S., Routh, P.S., Anno, P.D. & Castagna, J.P., 2005. Spectral decomposition of seismic data with continuous-wavelet transform, *Geophysics*, **70**, P19–P25.
- Stockwell, R.G., Mansinha, L. & Lowe, R.P., 1996. Localization of the complex spectrum: the S transform, *IEEE Trans. Signal Process.*, **44**(4), 998–1001.
- Taner, M.T., Koehler, F. & Sheriff, R.E., 1979. Complex seismic trace analysis, *Geophysics*, **44**(6), 1041–1063.
- Torres, M.E., Colominas, M.A., Schlotthauer, G. & Flandrin, P., 2011. A complete ensemble empirical mode decomposition with adaptive noise, in *Proceedings of 2011 IEEE International Conference on Acoustics, Speech and Signal Processing (ICASSP)*, pp. 4144–4147, IEEE.
- Wang, T., Zhang, M., Yu, Q. & Zhang, H., 2012. Comparing the applications of EMD and EEMD on time-frequency analysis of seismic signal, *J. appl. Geophys.*, **83**, 29–34.
- Wu, Z. & Huang, N.E., 2009. Ensemble empirical mode decomposition: a noise-assisted data analysis method, *Adv. Adapt. Data Anal.*, **1**, 1–41.
- Wu, X. & Liu, T., 2009. Spectral decomposition of seismic data with reassigned smoothed pseudo Wigner–Ville distribution, *J. appl. Geophys.*, **68**, 386–393.
- Xue, Y.-j., Cao, J.-x. & Tian, R.-f., 2013a. A comparative study on hydrocarbon detection using three EMD-based time-frequency analysis methods, *J. appl. Geophys.*, **89**, 108–115.
- Xue, Y.-j., Cao, J.-x., Wang, D.-x., Tian, R.-f. & Shu, Y.-x., 2013b. Detection of gas and water using HHT by analyzing P-and S-wave attenuation in tight sandstone gas reservoirs, *J. appl. Geophys.*, **98**, 134–143.

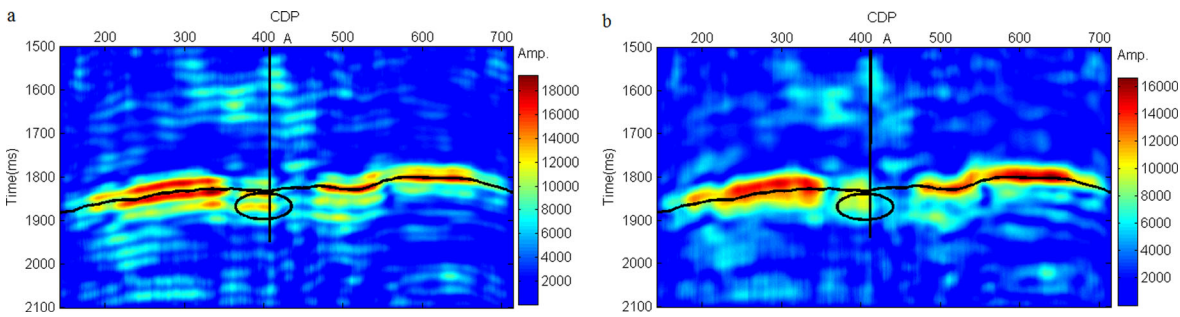


**Figure A1.** The common frequency section corresponding to the original seismic section in Fig. 6 calculated by STFT: (a) the 16 Hz common frequency section and (b) the 28 Hz common frequency section.

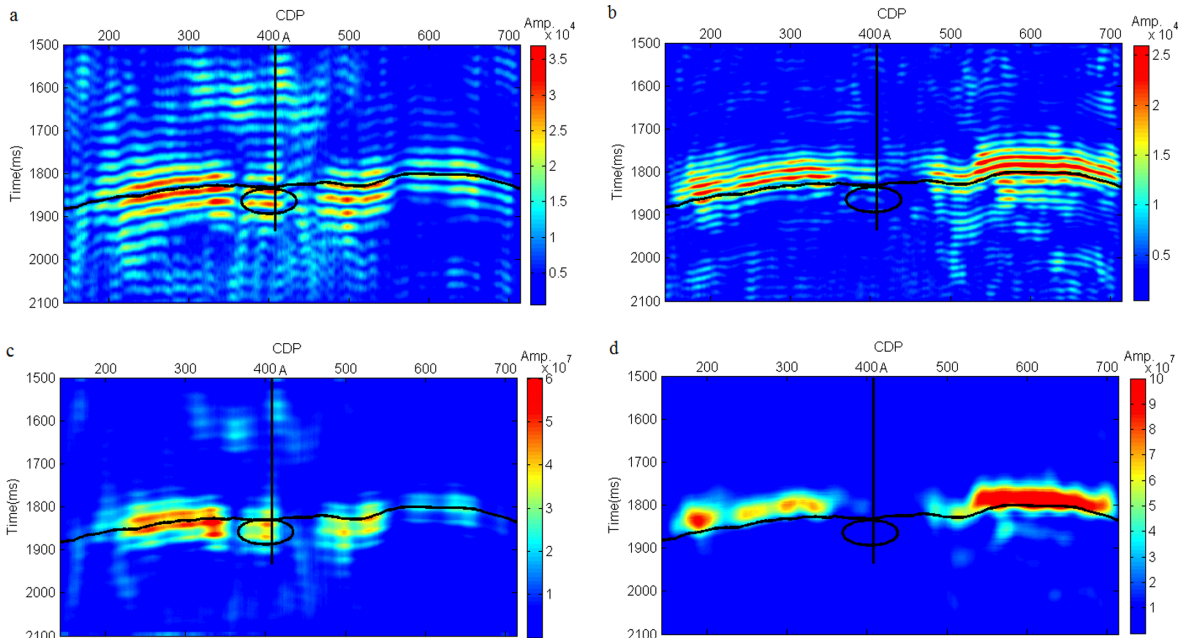


**Figure A2.** The common frequency section corresponding to the original seismic section in Fig. 6 calculated by CWT and the wavelet-transform TK energy method: (a) the 16 Hz common frequency section calculated by CWT, (b) the 28 Hz common frequency section calculated by CWT, (c) the 16 Hz common frequency section calculated by the wavelet-transform TK energy method and (d) the 28 Hz common frequency section calculated by the wavelet-transform TK energy method.

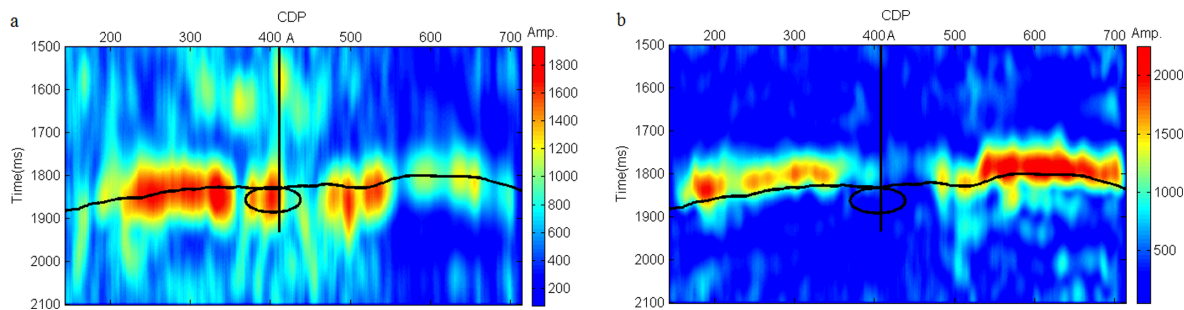
distinguish the events with high frequencies, but it ignores events with low frequencies. This section gives finer details. However, we find that the characteristics of the attenuation of high-frequency energy and the enhancement of low-frequency energy in Figs A1(a) and (b) are not especially clear, and its statistical interpretation is not good. Because STFT uses a fixed window function, as a time-frequency analysis method it has a fixed resolution. The time of the window function and the frequency resolution of STFT cannot be optimal simultaneously.

Fig. A2 shows the common frequency sections calculated by CWT (Figs A2a and b) and by the wavelet-transform TK energy method (Figs A2c and d). Here, a Morlet wavelet is used. In Figs A2(a) and (b), the events of the different common frequency sections are clear. The common frequency sections calculated by CWT give finer details than those calculated by STFT. The characteristics of the attenuation of high-frequency energy and the enhancement of low-frequency energy in Figs A2(a) and (b) are also clear. The wavelet transform uses a mobile scale-variable time window, and it allows the adaptive seismic trace acquisition to retain the effect better than STFT. However, the effectiveness of the wavelet

transform depends on the selection of the wavelet function. Sometimes the partial spectrum of the corresponding orthogonal basis functions becomes worse as the scale increases.

Figs A2(c) and (d) show a clearer statistical interpretations. The characteristics of the attenuation of high-frequency energy and the enhancement of low-frequency energy are excellent. At the same time, the common frequency sections calculated by the wavelet-transform TK energy method ignore the fine details. The wavelet-transform TK energy method calculates the TK energy of the scalogram obtained by the wavelet-transform, and its superior statistical interpretation of the common frequency section depends on the effect of the scalogram obtained by the wavelet-transform. Thus, the choice of the wavelet function will directly affect the effectiveness of the results.

The common frequency sections calculated by the *S* transform (Stockwell 1996) are shown in Fig. A3. The characteristics of the attenuation of high-frequency energy and the enhancement of low-frequency energy are clear. The common frequency sections calculated by the *S* transform also give a good statistical interpretation, but the temporal resolution is poor. In this method, the



**Figure A3.** The common frequency section corresponding to the original seismic section in Fig. 6 calculated by the S transform: (a) the 16 Hz common frequency section and (b) the 28 Hz common frequency section.

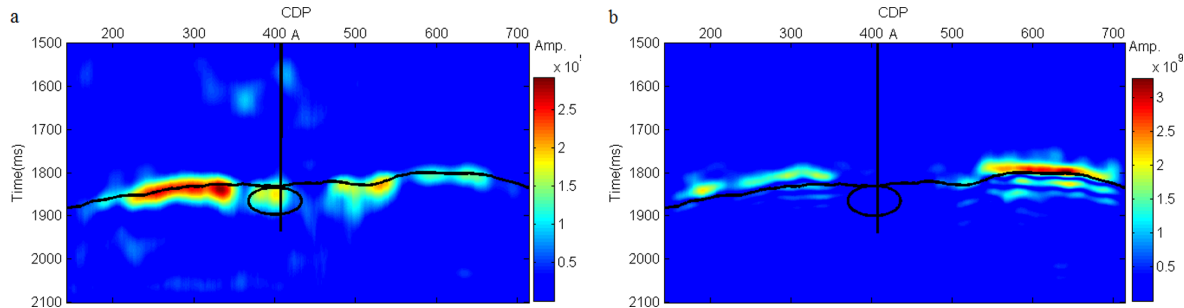


**Figure A4.** The common frequency section corresponding to the original seismic section in Fig. 6 calculated by the smoothed WVD: (a) the 16 Hz common frequency section and (b) the 28 Hz common frequency section.

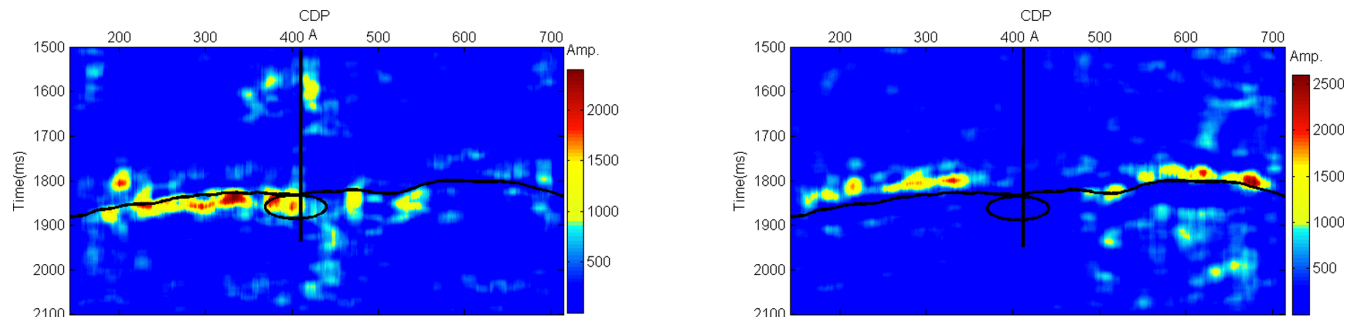


**Figure A5.** The common frequency section corresponding to the IMF2 section in Fig. 10(b) calculated by the HHT: (a) the 14–18 Hz common frequency section and (b) the 26–30 Hz common frequency section.

length of the time window depends on the frequency. The basic wavelet function of the Stockwell transform is fixed. In actual seismic signal processing, the characteristics of the time–frequency distribution are related not only to the signal itself but also to the seismic wavelet. It is difficult to use the fixed basic wavelet function in the Stockwell transform to meet the needs of the actual data processing.

Fig. A4 shows the common frequency sections calculated by the smoothed WVD. The characteristics of the attenuation of high-frequency energy and the enhancement of low-frequency energy are also clear. In this method, the cross-term interferences have been very good suppressions, but do not completely eliminate.

The introduction of the cross-term will lead to frequency artefacts in the time–frequency plane and will thus affect the resolution.

The common frequency sections calculated by the HHT are shown in Fig. A5. In Fig. A5(a), there are a larger energy in the objected area. In Fig. A5(b), the energy in the objected area is attenuated. However, for the analytic functions directly formed by the Hilbert transform (HT) of the IMF, according to Bedrosian theorem (Bedrosian 1963) and Nuttall theorem (Nuttall 1966), the scope of using HT to calculate the instantaneous characteristics of the signal is limited, especially for the complex modulated signals. Therefore the instantaneous attributes of some signals calculated by HHT method will produce unexplained phenomena.